AERO 520 INTRO. TO AEROSPACE DESIGN

Institute for Aerospace Eng. (Faculty of Engineering)

Winter 2026

Report #2

Introduction to Aircraft Aerodynamics

Evelyne Jewitt-Dyck: 261087480

Iris Sam Chacko: 261202510

Maverick Hoziel: 261115085

Milka Ininahazwe: 261214360

ABSTRACT

This report outlines the aerodynamic development and analysis of a premium business jet, building directly on the preliminary sizing results established in Report 1. The objective of this phase was to define the geometry of the wing and empennage and analyze the aircraft's aerodynamic characteristics using the Advanced Aircraft Analysis (AAA) software. To ensure high-speed cruise efficiency and delay onset of compressibility effects, a supercritical SC(2)-0612 airfoil was selected for the wing. For the empennage, NACA 0009 airfoils were implemented for both the horizontal and vertical tails to maintain control with minimal drag.

The analysis includes a comprehensive breakdown of the aircraft's geometry, spanwise lift distribution, and class II drag evaluating both parasitic and induced drag. Furthermore, the critical Mach numbers for the wing and tails were analyzed to verify performance at the design cruise speed.

TABLE OF CONTENTS

TABLE OF TABLES

TABLE OF FIGURES

1. WING

1.1. Airfoil Selection & Schematic

The wing airfoil selected for this preliminary design is the NASA SC(2)-0612 supercritical airfoil. This choice is primarily justified by the aircraft's high-subsonic cruise requirements, as supercritical airfoils are specifically designed to delay the onset of wave drag and increase the critical Mach number by flattening the upper surface pressure distribution, making them ideal in the transonic regime [1]. The "06" in the designation corresponds to a design lift coefficient (C_l) of 0.6, which aligns with the target cruise lift requirements identified in the Advanced Aircraft Analysis (AAA) flight condition data. A 12% thickness-to-chord ratio was selected to provide a balance between aerodynamic efficiency and the structural volume necessary for wing box reinforcement and fuel tank capacity. Verification through XFOIL at a Reynolds number of 3 x 10^6 confirms a zero-lift angle of attack ($\alpha_{L=0}$) of -3.8222° and a stable pitching moment (C_M) of -0.1049, ensuring predictable longitudinal behavior within the linear lift range.

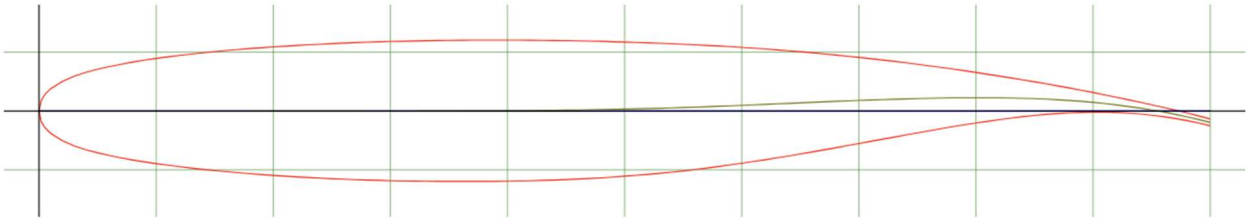

Figure 1: NASA SC(2)-0612 airfoil

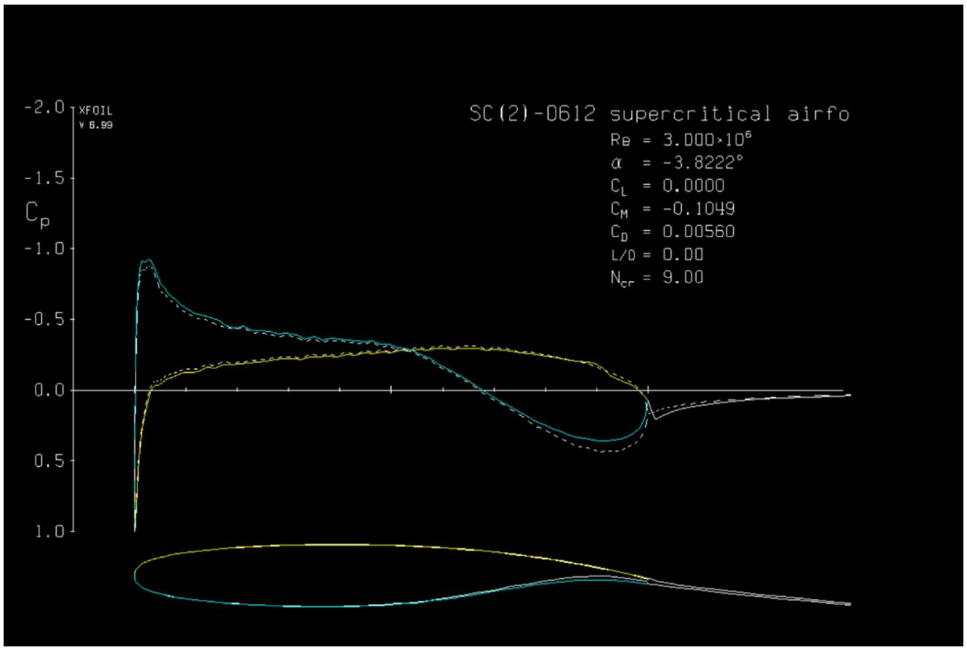

Figure 2: Xfoil SC(2)-0612 Airfoil Simulation

1.2 Airfoil 2D Cl_alpha

The C_L versus angle of attack (α) curve for the selected airfoil was simulated using Flow5 (XFLR5) [2]. A Reynolds number of 1×10^6 was used for the simulations, whereas XFOIL analyses were previously performed at 3×10^6. The higher Reynolds number produced inconsistent results within Flow5, while simulations at 1×10^6 demonstrated improved numerical stability and more reliable aerodynamic trends. The resulting C_L versus α curve is shown in Figure 3.

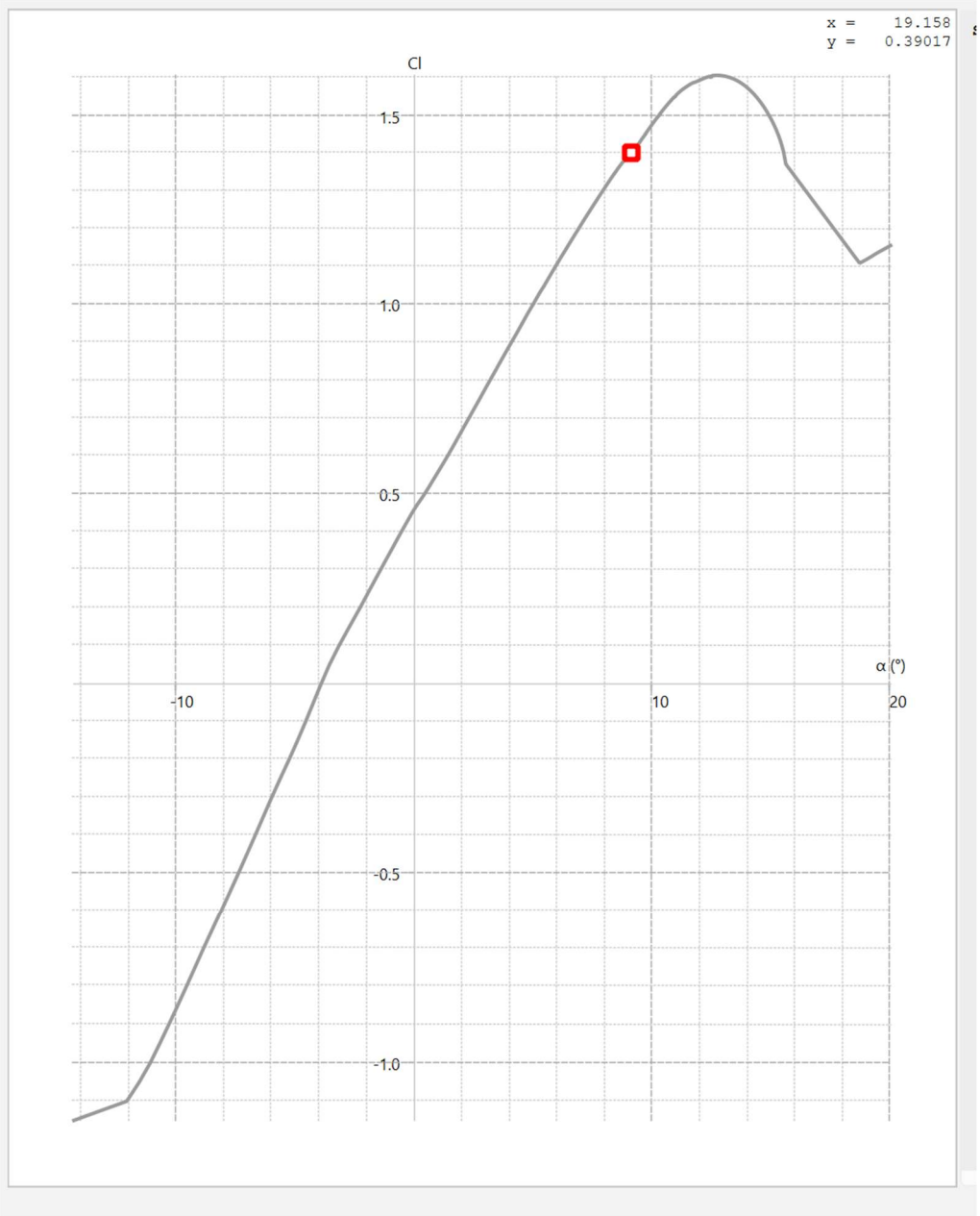

Figure 3: Lift Coefficient Versus AOA for SC(2)-0612 Airfoil

Furthermore, analysis of the tabulated data points allowed the determination of the linear-region slope of the curve. The data used to calculate the slope are presented in Figure 4 below.

SC(2)-0612 supercritical airfoil

T1-Re1.000-N9.0

	α (°)	Cl	Cd
103	4.2	0.915231	0.0124876
104	4.3	0.926196	0.012592
105	4.4	0.937532	0.0126385
106	4.5	0.948843	0.0126902
107	4.51134	0.95	0.0126982
108	4.6	0.96011	0.0127502
109	4.7	0.971295	0.0128245
110	4.8	0.982291	0.0129122
111	4.9	0.992962	0.0130333
112	4.96917	1	0.0131532
113	5	1.00359	0.0131643
114	5.1	1.01468	0.0132217
115	5.2	1.02563	0.0133016
116	5.3	1.03633	0.0134192
117	5.4	1.0462	0.0136766
118	5.44056	1.05	0.0137929
119	5.5	1.0566	0.013851
120	5.6	1.06737	0.0139628
121	5.7	1.07807	0.0140856
122	5.8	1.08873	0.0142175
123	5.9	1.09934	0.0143568
124	5.90791	1.1	0.0143703
125	6	1.10986	0.0144969
126	6.1	1.12026	0.014638
127	6.2	1.13062	0.0147848
128	6.3	1.14095	0.0149362
129	6.39012	1.15	0.0150788

Figure 4: Lift Coefficient Versus AOA for SC(2)-0612 Airfoil Table Data

The linear lift-curve slope was calculated using the following relation:

$$slope = \frac{\Delta C_L}{\alpha}$$

$$slope\ (^{\circ -1}) = \frac{1.15 - 0.915231}{6.39012 - 4.2} = 0.107^{\circ -1}$$

$$slope(rad^{-1}) = 0.107 * \frac{180}{\pi} = 6.14\ rad^{-1}$$

This lift-curve slope was then implemented in the AAA Airfoil Lift versus Angle of Attack input section, as shown in Figure 5.

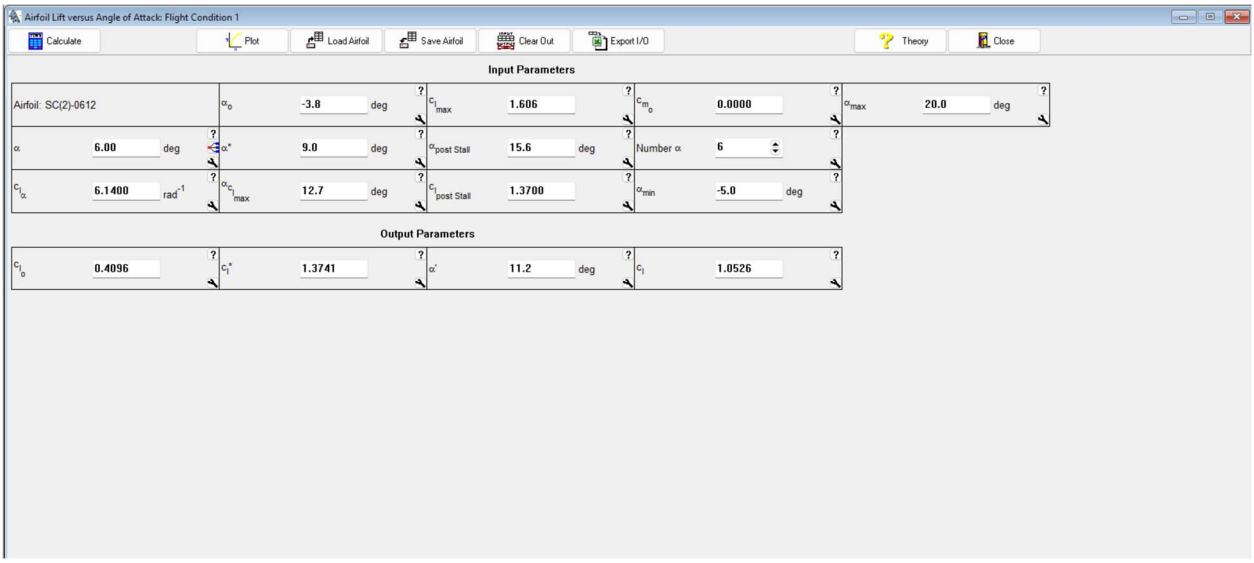

Figure 5: SC(2)-0612 Airfoil Lift Versus AOA

The resulting C_L vs. α curve generated in AAA is shown in Figure 6 below.

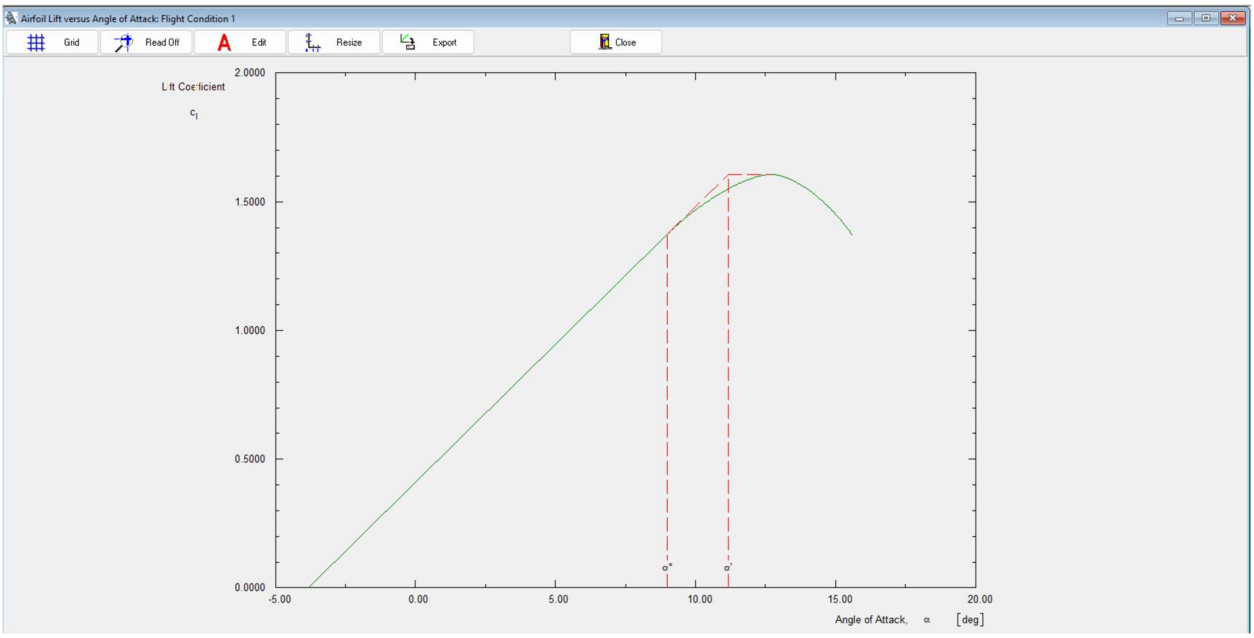

Figure 6: Lift Coefficient Versus AOA From AAA

This C_L vs. α plot shows good agreement with the results previously obtained from Flow5. Additionally, Flow 5 confirmed the zero-lift angle of attack α of approximately –3.9, only –0.1 difference with the value calculated by XFoil. The raw value is shown in Figure 7 below. This shows consistency of our analysis across all three softwares.

SC(2)-0612 supercritical airfoil

T1-Re1.000-N9.0

	α (°)	Cl
21	-4.9169	-0.15
22	-4.57689	-0.1
23	-4.25058	-0.05
24	-3.92436	2.98022e-08
25	-3.57934	0.05

Figure 7: Zero-Lift Angle of Attack from Flow5

Additionally, the Flow5 software was used to generate the C_L vs. C_D curve, commonly referred to as the drag bucket. The resulting drag bucket graph is shown in Figure 8 below.

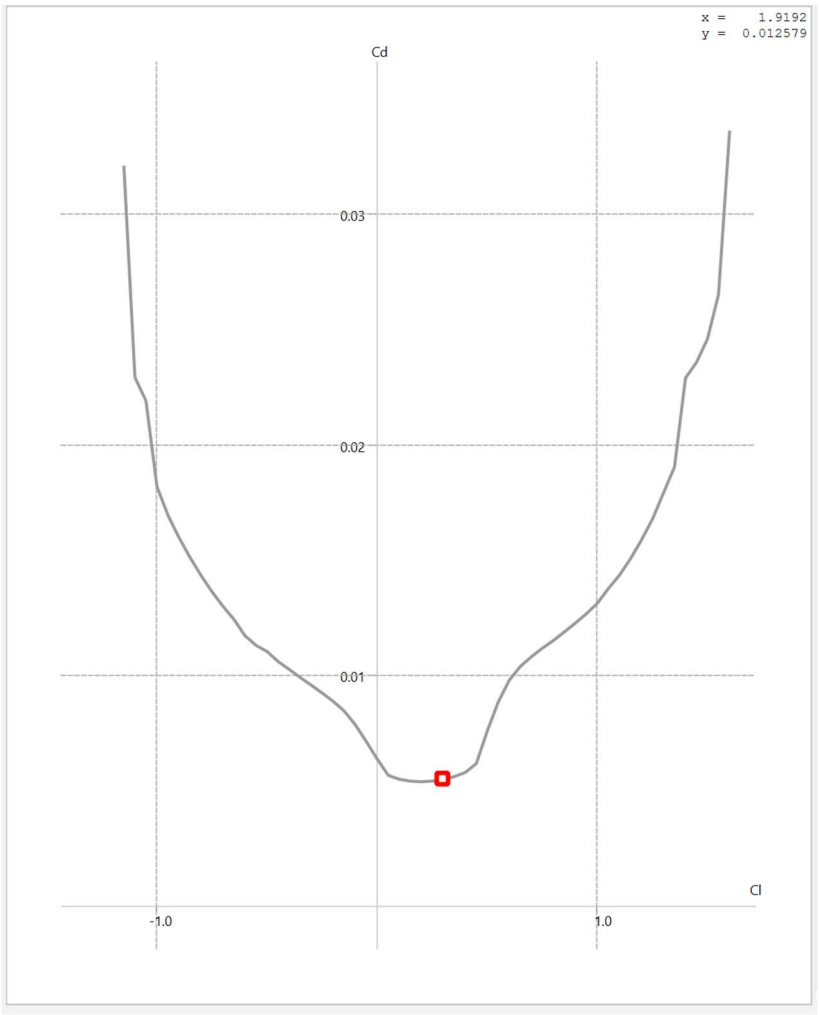

Figure 8: SC(2)-0612 Airfoil Low Speed Drag Bucket

This graph indicates that the optimal operating C_L range lies approximately between 0.1 and 0.6, corresponding to the low-drag region commonly referred to as the drag bucket [3]. Although the simulations were performed at low Mach numbers (0.10–0.20) and a Reynolds number of 1×10^6, the presence of a broad low-drag region is consistent with the expected behavior of a supercritical airfoil such as the SC(2)-0612. This supports the selected operating condition near $C_L\approx0.6$.

1.3 Wing Geometry Table & Schematic

The wing geometry inputs and resulting outputs are presented in Figure 9 below.

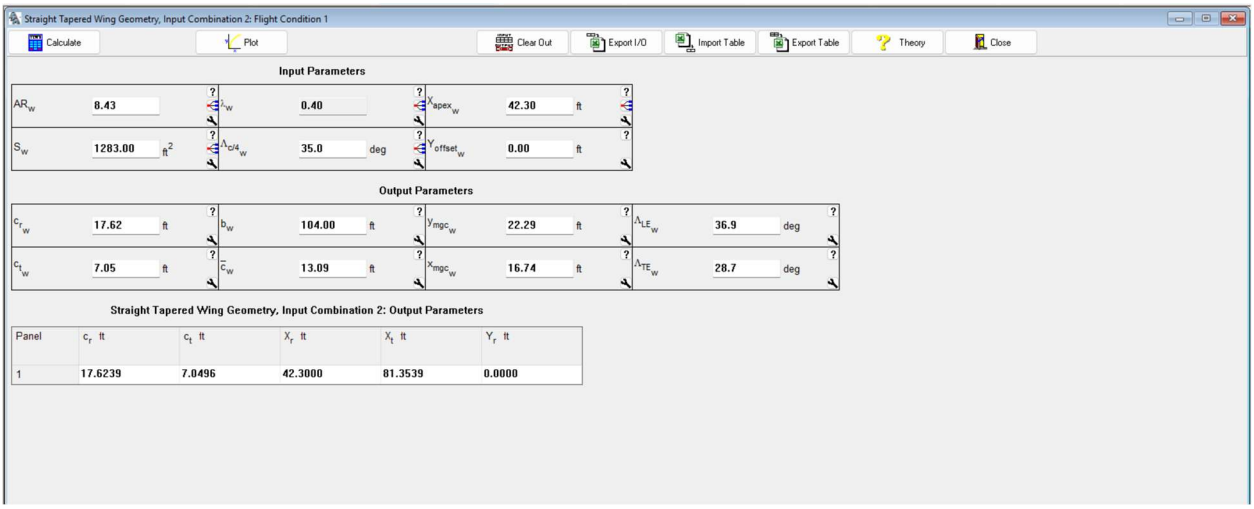

Figure 9: Wing Geometry Table

Originally, the wing taper ratio was selected based on measurements obtained from a CAD model of the Gulfstream G700 [4], resulting in an initial value of 0.234. Detailed geometric parameters such as taper ratio and exact sweep angle are not typically published in publicly available aircraft data sources, particularly for modern long-range ultra-premium business jets. Consequently, the referenced CAD model [4] was used as the most representative available geometric reference for benchmarking purposes. A wing sweep angle of 35 degrees was similarly adopted from this model. Additionally, high subsonic transport aircraft typically employ quarter-chord wing sweep angles in the range of approximately 30° to 37°, as this level of sweep delays the onset of compressibility effects and reduces wave drag at transonic cruise speeds [6].

However, the resulting lift distribution analysis indicated a tendency toward tip stall, which is undesirable from both stability and controllability perspectives. An iterative refinement process was therefore conducted, during which the taper ratio and geometric twist were adjusted to achieve a more favorable spanwise lift distribution. A taper ratio of 0.4 was ultimately identified as the minimum value that mitigated the risk of tip stall while remaining close to the initial design baseline. In addition, a geometric wing twist angle of −5 degrees was selected to further

improve the lift distribution, as shown in Figure 10. Further discussion of these adjustments is provided in the lift distribution section.

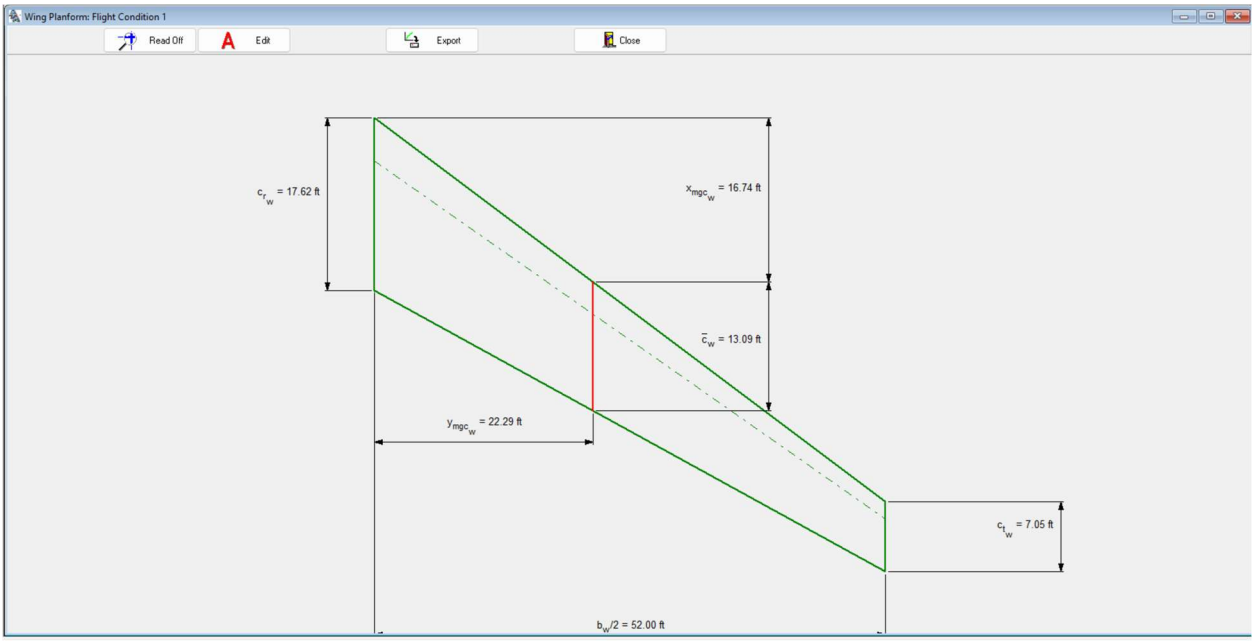

Figure 10: Wing Geometry Schematic

1.4 Wing Twist

The wing geometric twist angle was chosen to be -5 degrees as shown below in Figure 11.

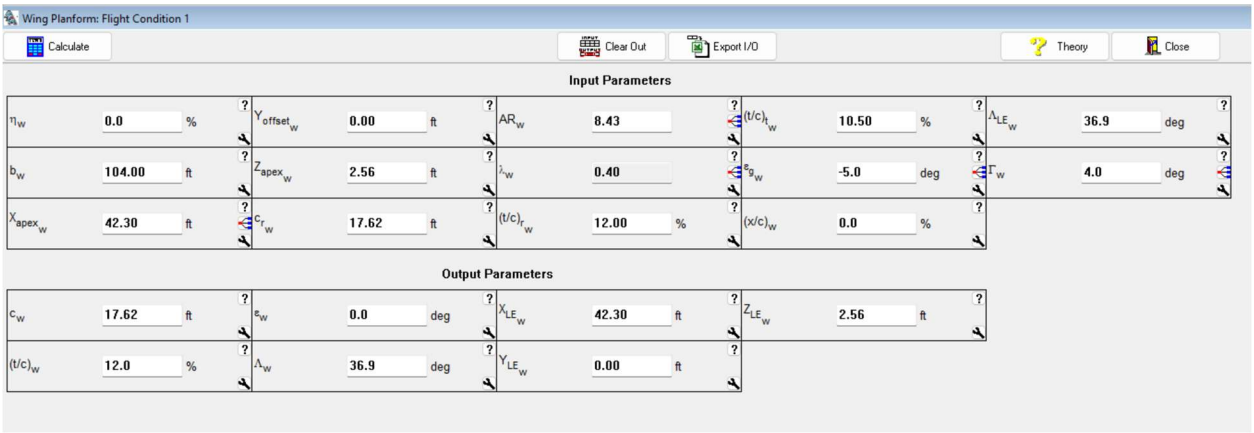

Figure 11: Wing Planform Inputs & Outputs

The choice of geometric twist was guided by analysis of the lift distribution curve. It was determined that the twist angle required a minimum magnitude of −5 degrees to achieve the desired lift distribution and mitigate undesirable aerodynamic behavior such as tip stall. Less negative values (e.g., −3° or −2°) were found to be insufficient. Further discussion is provided in the lift distribution section.

1.5 Lift Distribution Spanwise

This section had a significant influence on several aircraft design parameters, as the initially selected configuration indicated a potential tendency toward tip stall during lift distribution analysis. As mentioned previously, both the taper ratio and the wing geometric twist angle were refined based on the lift distribution results, with the primary objective of achieving a more favorable spanwise loading and avoiding premature tip stall.

With the original values of a taper ratio of 0.234 and a geometric twist angle of −3 degrees, the lift distribution showed a peak near 75–80% of the wingspan, indicating an increased risk of tip stall. This behavior is illustrated in Figure 12.

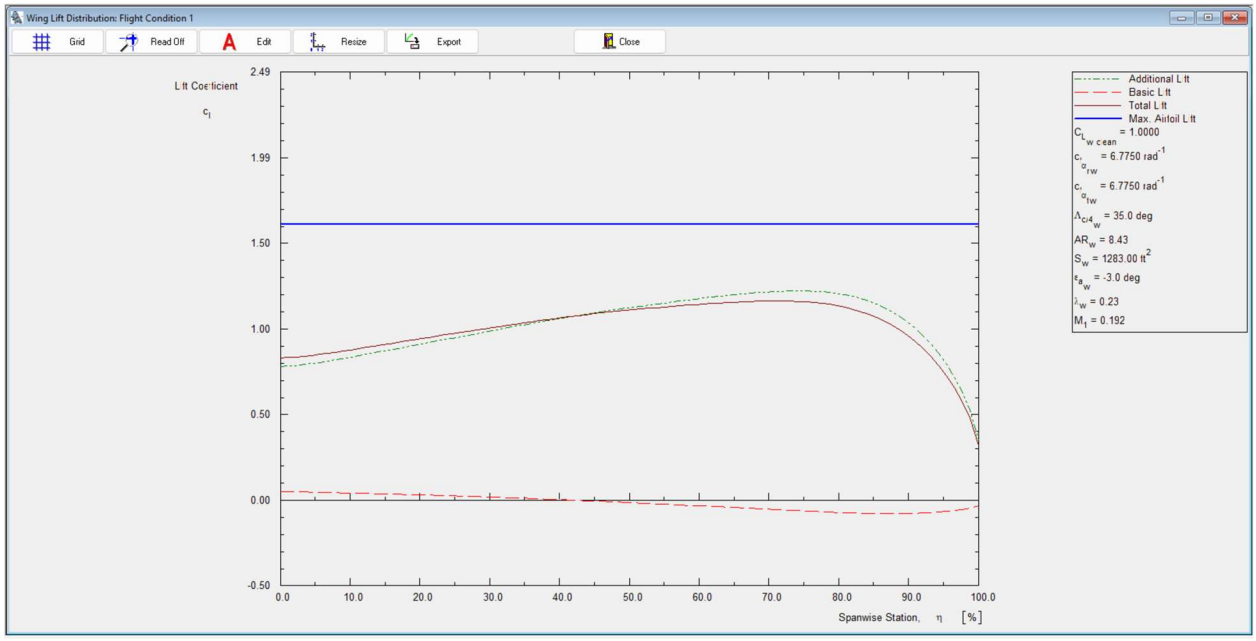

Figure 12: High Risk of Tip Stall Lift Distribution

To mitigate the risk of tip stall, achieving a favorable lift distribution became a primary design objective, requiring adjustments to previously established parameters. Through iterative refinement of the taper ratio and wing geometric twist angle, the lift distribution was progressively improved by increasing the taper ratio and introducing greater geometric washout. A taper ratio of 0.4 combined with a wing geometric twist angle of −5 degrees was ultimately selected, as this configuration minimized the likelihood of tip stall while remaining as close as possible to the original design intent.

Figures 13 and 14 illustrate the resulting lift distribution, which shows a peak lift located near approximately 50% of the wingspan, indicating a more desirable spanwise loading [3].

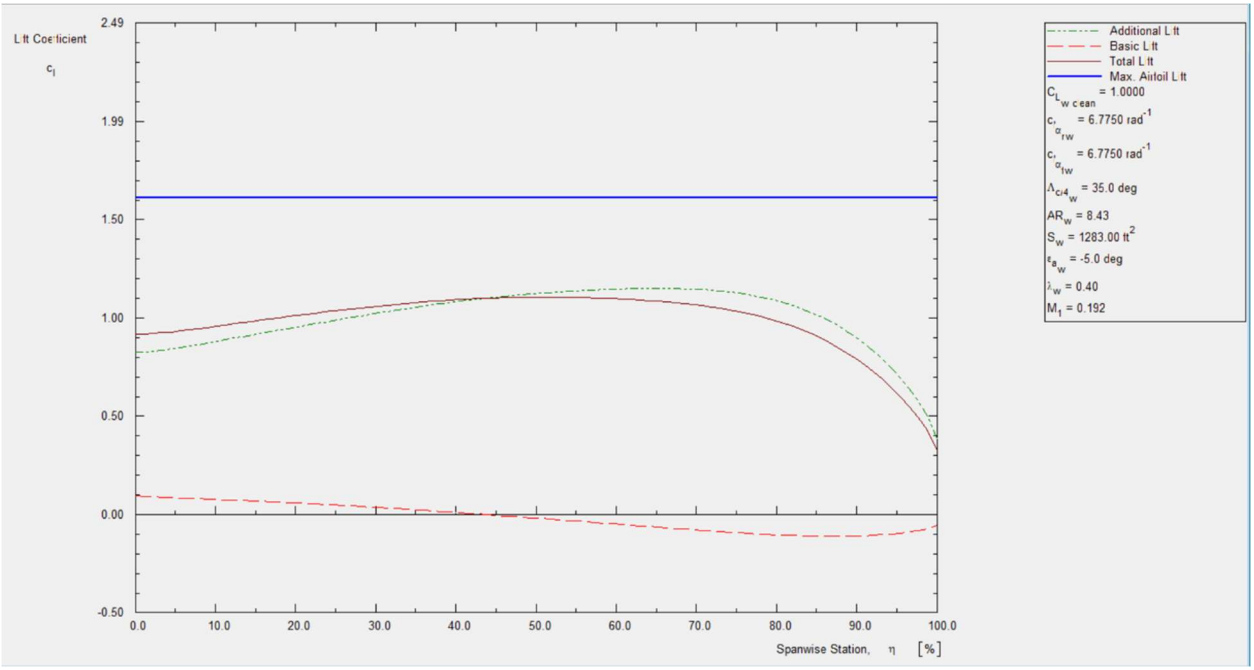

Figure 13: Desirable Lift Distribution

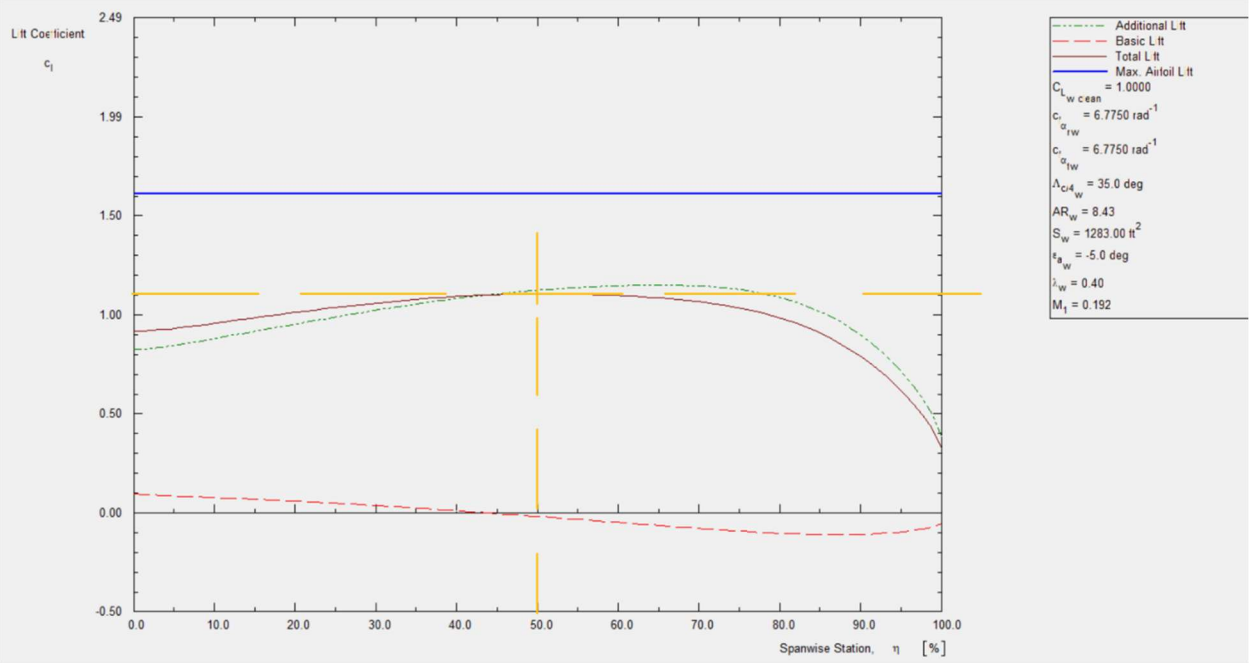

Figure 14: Lift Distribution Plot Annotated at 50% Span

It is important to note that the flight condition selected for this analysis corresponds to the landing phase. Since tip stall is more likely to occur at low speeds and high angles of attack [5], the lift distribution was evaluated under landing conditions. An altitude of 0 ft and a speed of 127 knots, corresponding to the aircraft's clean stall speed, were used for the analysis. Although landing would typically be performed with flaps deployed, resulting in a lower stall speed of approximately 104 knots, the clean stall speed was intentionally selected as a conservative reference condition. Also, a landing weight of 72053.7lb was selected from the initial weight sizing. These parameters are shown in Figure 15 below.

Figure 15: Flight Condition Definition

2. HORIZONTAL TAIL

2.1. Airfoil Selection

The airfoil selected for the horizontal tail is the NACA 0009[6], a 9% thick symmetrical airfoil. This choice is primarily driven by the requirement for a low-drag, high-efficiency surface that provides consistent aerodynamic characteristics across a wide range of angles of attack [7]. Unlike the main wing, which uses a cambered supercritical airfoil to generate lift at zero alpha, the horizontal tail must maintain neutral stability and minimize parasitic drag during cruise [7]. The 9% thickness-to-chord ratio offers a significant reduction in profile drag compared to the wing's 12% thickness, while still providing sufficient structural volume for internal spars and elevator actuators [7]. Furthermore, the symmetrical nature of the NACA 0009 ensures that the tail produces no lift at zero degrees of incidence, allowing the aircraft's longitudinal trim to be precisely managed by the elevator and tail incidence settings without introducing unnecessary camber-related drag [7]. The airfoil geometry and the C_l vs. α graph are presented in figures 16 and 17 below.

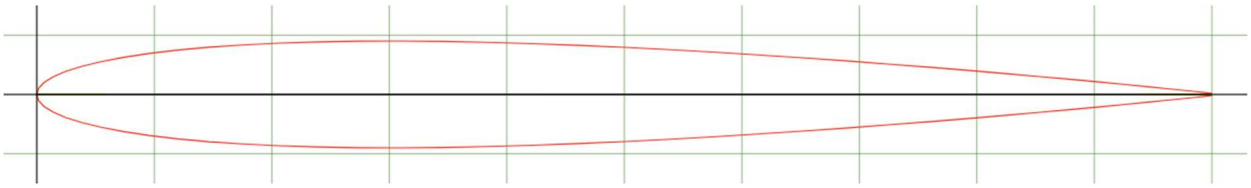

Figure 16: Naca 0009 airfoil Plot (airfoil tools)

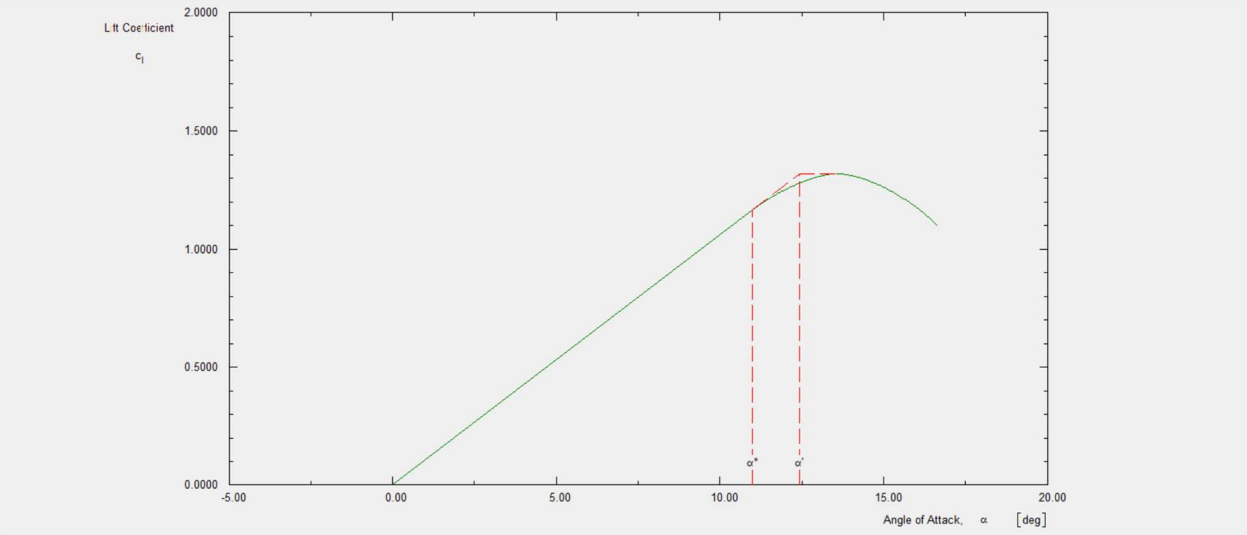

Figure 17: CL vs Alpha for NACA 0009

2.2. Horizontal tail planform

The horizontal tail geometry was defined using a planform modeled for high-speed stability and control effectiveness, as shown in the Advanced Aircraft Analysis (AAA) output. The horizontal tail features a span (b_h) of 34.12 ft and a root chord (c_{rh}) of 10.17 ft, resulting in an aspect ratio (AR_h) of 4.16. A taper ratio (λ_h) of 0.61 was selected to balance structural weight with aerodynamic efficiency [7]. To maintain aerodynamic integrity at high-subsonic Mach numbers, the leading edge is swept at 25.9 degrees (Λ_{LEh}), which delays compressibility effects on the tail surfaces [7]. The profile utilizes the NACA 0009 symmetrical airfoil with a constant 9% thickness-to-chord ratio ($(t/c)_h$) across the span. Additionally, the tail is set at a zero-degree twist (ε_h) and zero-degree dihedral (Γ_h), ensuring neutral aerodynamic characteristics that simplify longitudinal trim adjustments throughout the flight envelope [7]. The following table 1 shows the parameters and the figures that follow shows the AAA inputs and the Horizontal tail geometry plot.

Table 1: Horizontal Tail Geometry Parameters

Parameters	Values
Horizontal tail area (S_h)	279.61 ft
Tapper ratio (λ_h)	0.61
Aspect ratio (AR_h)	4.16
Span (b_h)	34.12 ft

Root Chord (c_{rh})	10.17 ft
Tip Chord (c_{th})	6.22 ft
Mean geometric chord ($\bar{c}_h$)	8.35 ft
Quarter chord Sweep ($\Lambda_{\frac{c}{4}_h}$)	23.2°
Leading Edge Sweep (Λ_{LE_h})	25.9°
Thickness to chord ratio ($(t/c)_h$)	9%
Twist Angle (ε_h)	0
Dihedral Angle (Γ_h)	0

The primary geometric parameters for the horizontal tail were calculated to ensure adequate longitudinal control and stability. Figure 18 presents the final output from the Advanced Aircraft Analysis (AAA) geometry module, documenting the resulting surface area and the chord lengths.

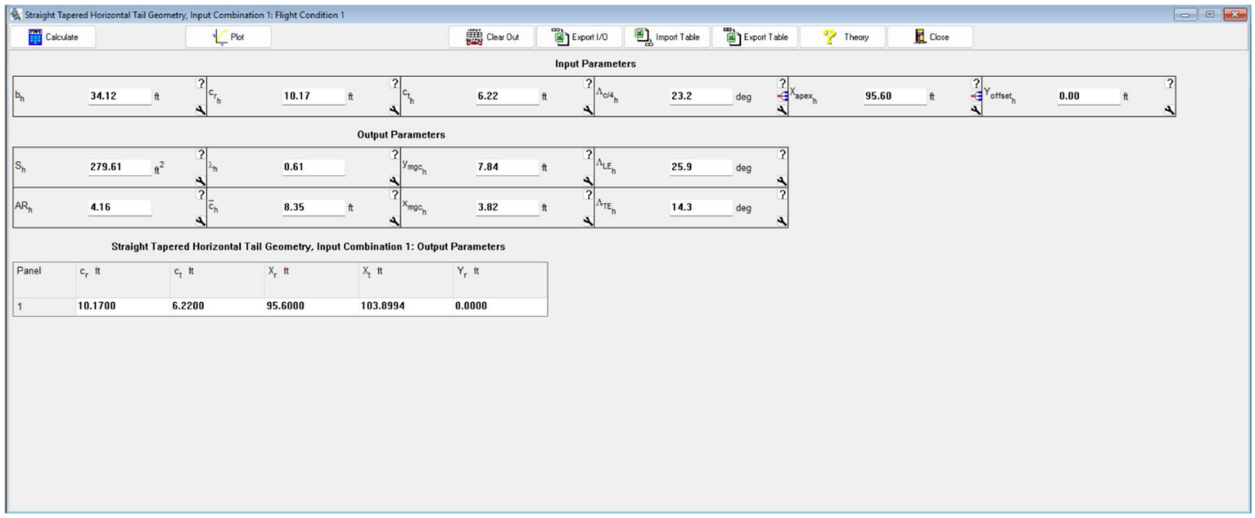

Figure 18: Sraight tapered horizontal tail geometry

Figure 19 displays the planform condition within the software environment, illustrating the relative positioning of the 23.2° quarter-chord sweep required for high-speed cruise.

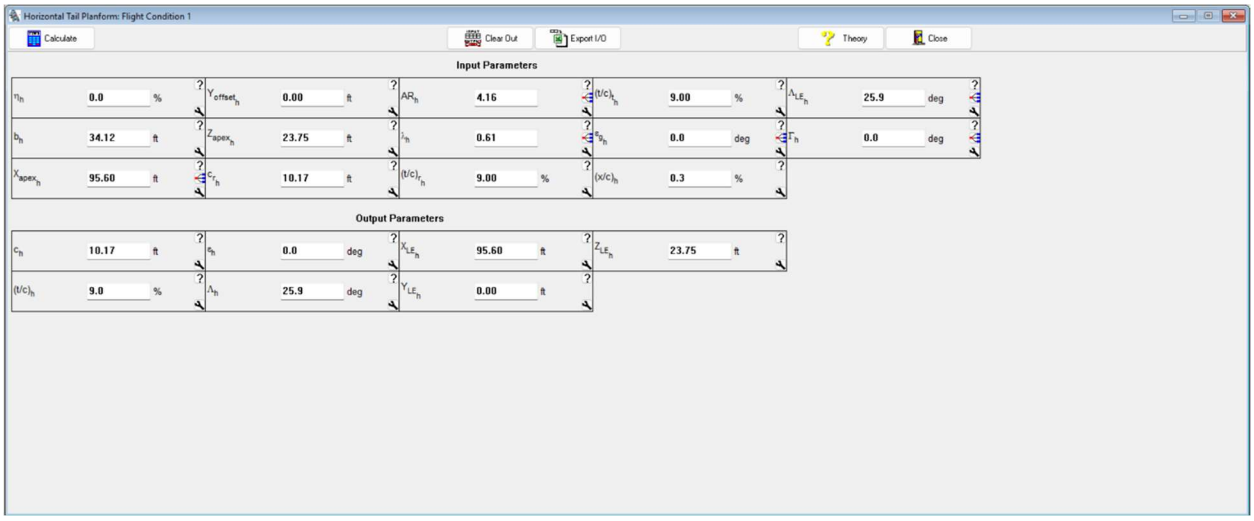

Figure 19: Horizontal tail planform condition

Figure 20 illustrates the straight-tapered geometry.

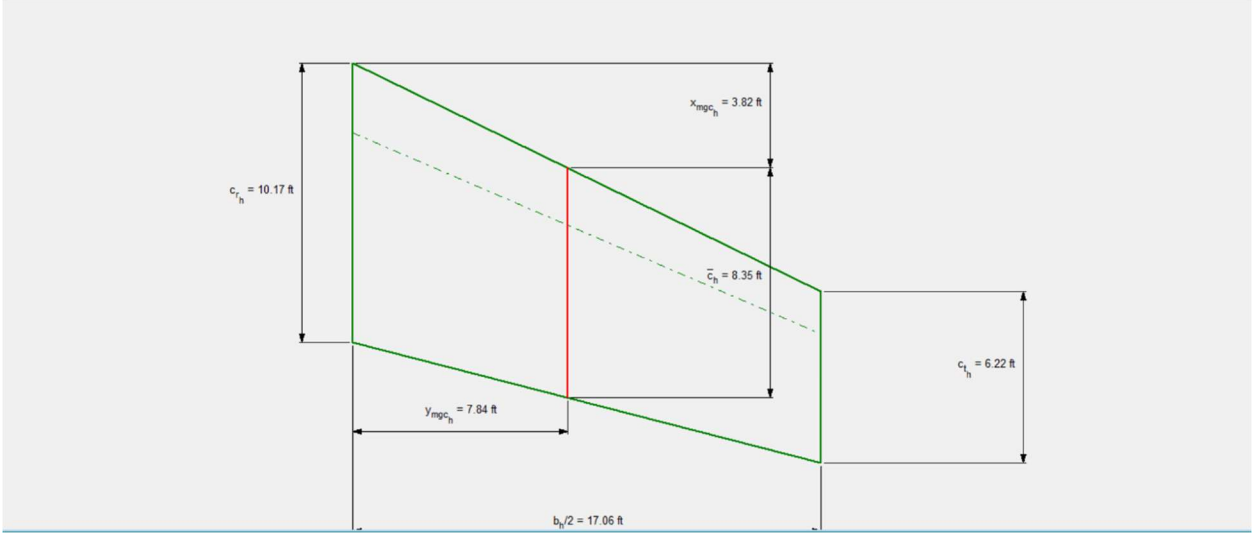

Figure 20: Horizontal tail geometry plot

2.3. Horizontal Tail Aerodynamics

The three-dimensional lift characteristics of the horizontal tail were calculated in Advanced Aircraft Analysis (AAA) to account for the finite aspect ratio (AR_h=4.16) and sweep of the planform. Based on the NACA 0009 airfoil properties, the 3D lift curve slope ($C_{l\alpha h}$) is determined in AAA software to be 6.0722 rad^{-1} for incompressible flow. Accounting for compressibility effects at moderate speeds, the slope increases to 7.1349 at Mach 0.6. Furthermore, the maximum three-dimensional lift coefficient ($C_{lmax,h}$) for the horizontal stabilizer

is established at 1.319 as we get the same $C_{lmax,rh}$ & $C_{lmax,th}$, with a corresponding stall angle ($\alpha_{h,Clmax,h}$) of 13.6°. Table 2 provides the calculated values for 3d lift parameters.

Table 2: Horizontal tail Aerodynamics

Parameter	Value
3D Lift Curve Slope ($C_{l_{\alpha h@M=0}}$)	6.0722 rad^{-1}
3D Lift Curve Slope $C_{l_{\alpha h@M=0.6}}$)	7.1349 rad^{-1}
Max 3D Lift Coefficient ($C_{lmax,h}$)	1.319
Stall Angle ($\alpha_{h,Clmax}$)	13.6°

Figure 21 shows the calculated aerodynamics values for the horizontal tail.

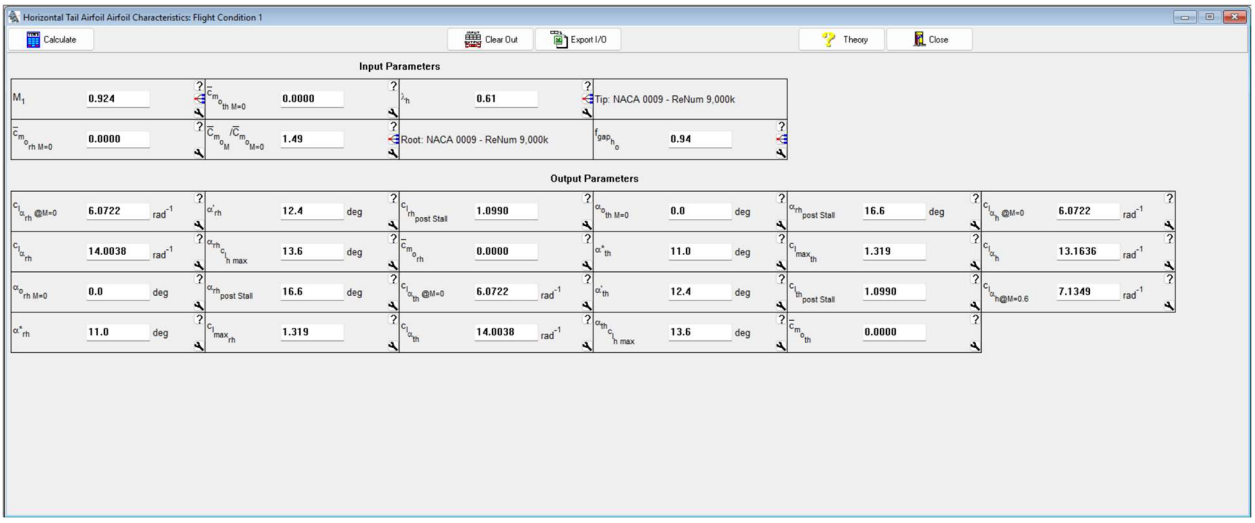

Figure 21: AAA Horizontal Tail 3D Aerodynamic Coefficients

3. VERTICAL TAIL

3.1. Airfoil Selection

The NACA 0009 was also selected for the vertical tail to ensure optimal directional stability and control. One of the basic aircraft design requirements is symmetry about the xz plane. Therefore, to ensure symmetry of the aircraft about the xz plane, the vertical airfoil section must be symmetric [8]. The thin 9% profile is particularly advantageous for the vertical tail as it delays the onset of compressibility effects at high Mach numbers [7]. By using a common airfoil for both the horizontal and vertical surfaces, the design also benefits from simplified manufacturing and aerodynamic modeling consistency across the tail assembly. The airfoil geometry and 2d Alpha plot is similar to the plot in Section 2.1. The airfoil geometry and C_l x α curves are shown in Figures 22 and 23 respectively.

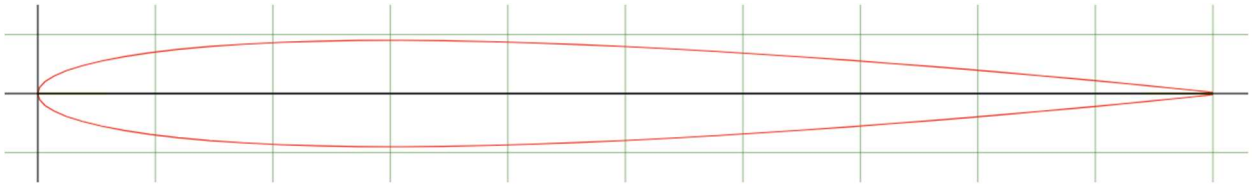

Figure 22: Naca 0009 airfoil Plot (airfoil tools)

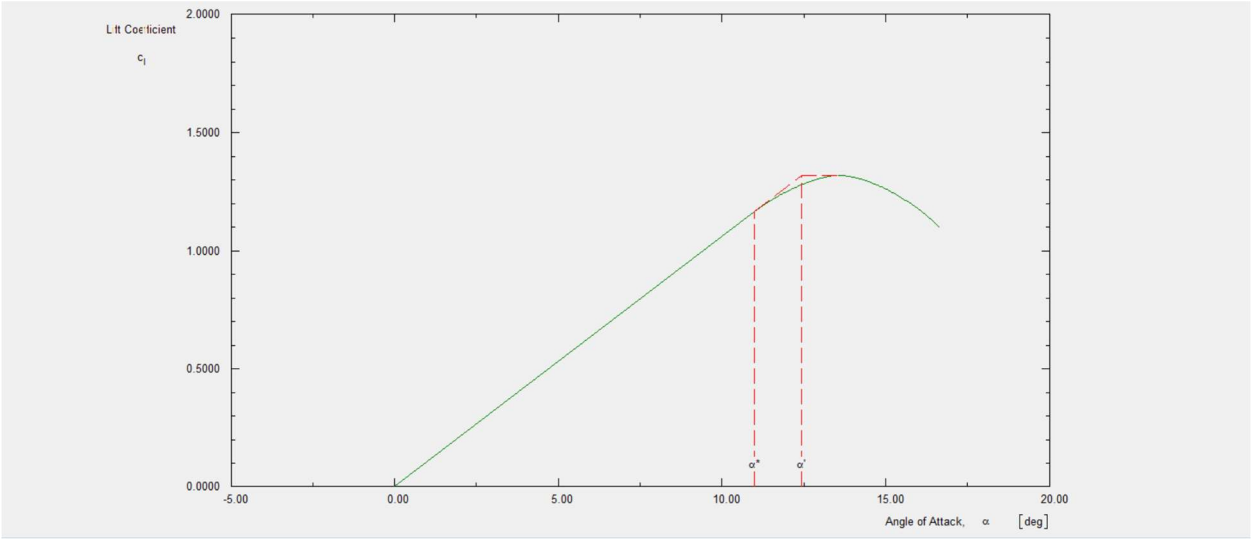

Figure 23: CL vs Alpha for NACA 0009

3.2. Vertical tail planform

The vertical tail geometry was established to provide the necessary directional stability and yaw control, utilizing a straight-tapered planform as shown in the Advanced Aircraft Analysis (AAA) output. The vertical tail has a total surface area (S_v) of 158.88 and a span (b_v) of 13.12 ft,

resulting in an aspect ratio (AR_v) of 1.08. The geometry features a root chord (c_{rv}) of 15.03 ft and a tip chord (c_{tv}) of 9.19 ft, corresponding to a taper ratio (λ_v) of 0.61. The quarter-chord sweep ($\Lambda_{\frac{c}{4}v}$) is set at 37.8 degrees, with a leading-edge sweep (Λ_{LE_v}) of 41.6 degrees.

The specific geometric parameters used to model the vertical tail are detailed in Table 3, with the corresponding software input and output environment captured in Figure 24.

Table 3: Vertical Tail planform geometry parameters

Parameters	Values
Horizontal tail area (S_v)	158.88 ft
Tapper ratio (λ_v)	0.61
Aspect ratio (AR_v)	1.08
Span (b_v)	13.12 ft
Root Chord (c_{rv})	15.03 ft
Tip Chord (c_{tv})	9.19 ft
Mean geometric chord ($\bar{c}_v$)	12.34 ft
Quarter chord Sweep ($\Lambda_{\frac{c}{4}v}$)	37.8°
Leading Edge Sweep (Λ_{LE_v})	41.6°
Thickness to chord ratio ($(t/c)_v$)	9%
Twist Angle (ε_v)	0
Dihedral Angle (Γ_v)	0

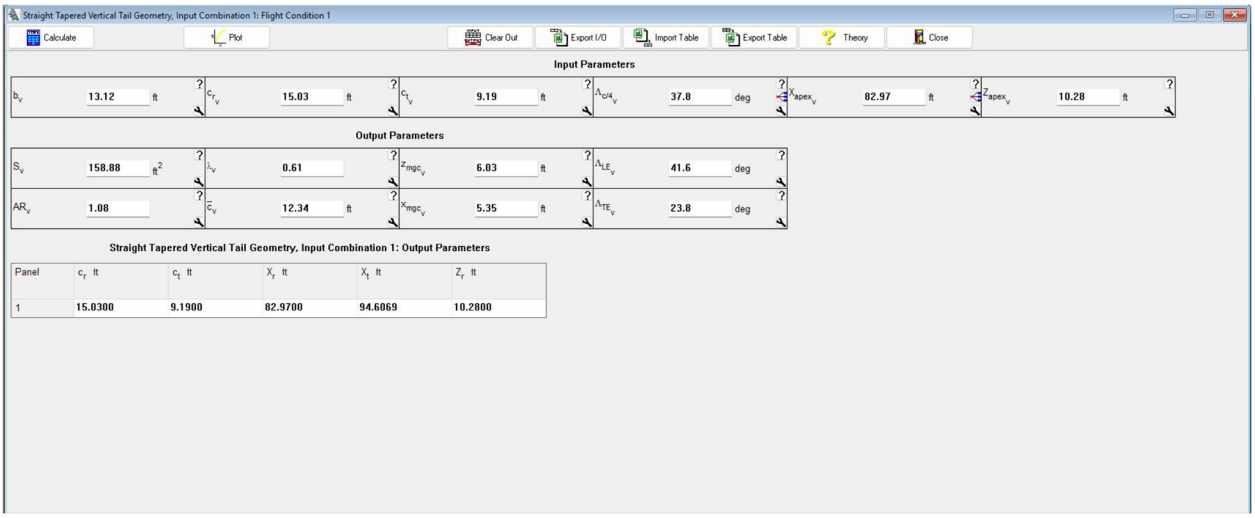

Figure 24: AAA Straight Tapered Vertical Tail Geometry Output

Figure 25 displays the planform condition as defined in the Advanced Aircraft Analysis (AAA) environment.

Figure 25: Vertical Tail Planform condition

Figure 26 presents the final vertical tail geometry.

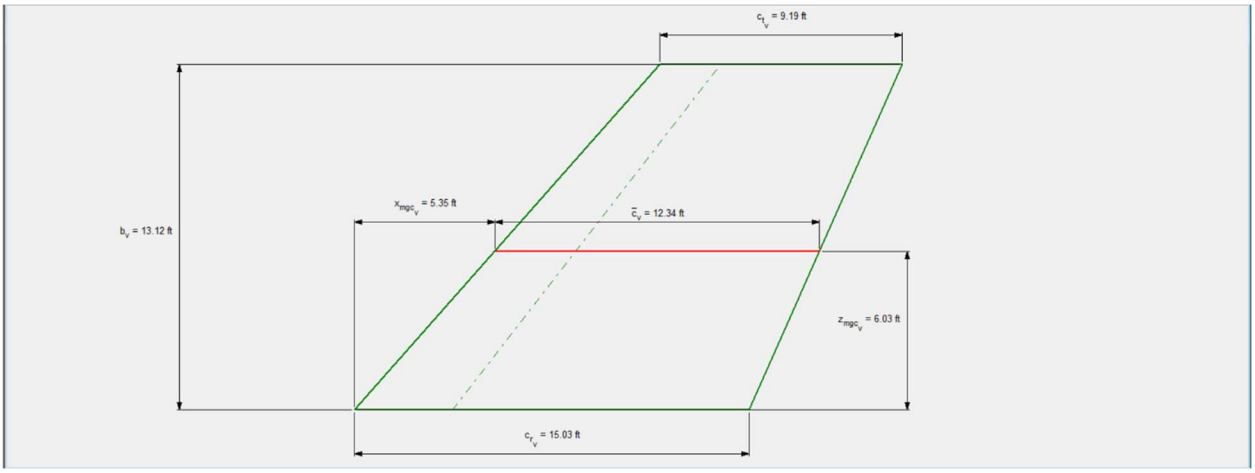

Figure 26: Vertical tail geometry plot

4. DRAG CALCULATION

4.1. Wing

The wing is the primary source of drag for the aircraft [10], characterized by an area (S_w) of 1283 ft^2 and an aspect ratio (AR_w) of 8.43. The planform geometry is further defined by a taper ratio (λ_w) of 0.40 and a quarter chord ($\Lambda_{c/4_w}$) of 35.0 degrees. The total wetted area of the wing (S_{wet_w}) is 2751 ft^2, and the surface finish is modeled with a sand roughness (k_{sand}) of 0.000016 ft.

At a turbulent Reynolds number ($Re_{w_{tur}}$) of 1,413,262.9, the wing achieves a skin friction coefficient (C_{f_w}) of 0.0019. When integrated with the form drag derived from the 12% thickness-to-chord ratio ($(t/c)_w$), the resulting zero-lift drag coefficient ($C_{D_{o_w}}$) is 0.0051.

Furthermore, at the analyzed lift coefficient (C_{L_w}) of 1.70, the wing generates a lift-dependent drag coefficient ($C_{D_{L_w}}$) of 0.1216. The efficiency of the wing is characterized by an Oswald efficiency factor (e_w) of 0.9198, confirming the effective minimization of induced drag for this jet configuration. All these parameters are summarized as both inputs and outputs in Figure 27 below, incorporating previously established design values.

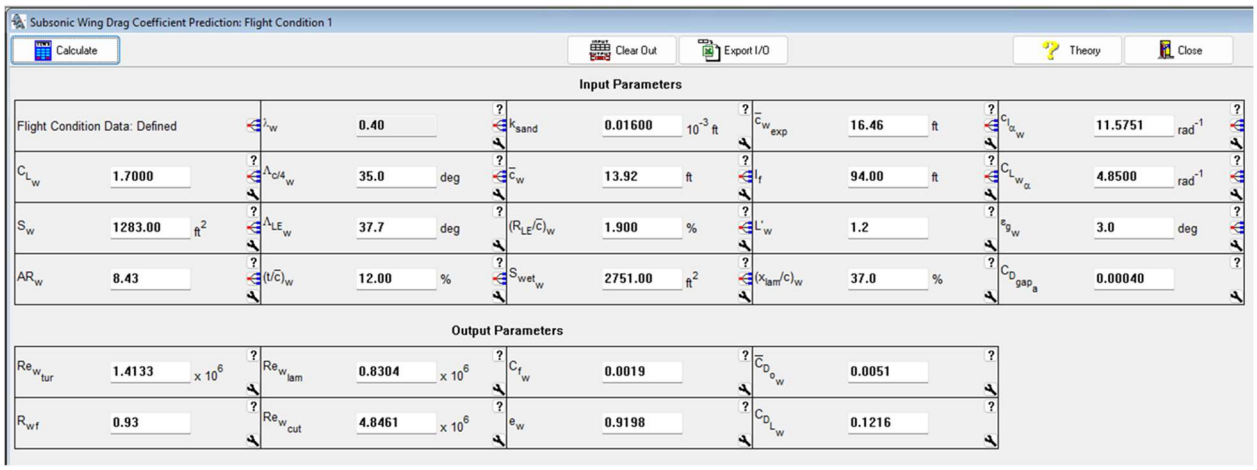

Figure 27:Subsonic Wing Drag Coefficient Prediction

4.2. Fuselage

The fuselage drag analysis is characterized by the aerodynamic interaction of the long, slender body required for an ultra-premium cabin and the high-speed cruise requirements. The fuselage has a total length (l_f) of 110.00 ft and a maximum diameter ($D_{f_{max_w}}$) of 9.35 ft. The analysis assumes a fully turbulent boundary layer development along the entire length of the airframe. The fuselage operates at a high Reynolds number, resulting in a skin friction coefficient (C_{f_f}) of 0.0019. This coefficient represents the viscous resistance of the air as it remains attached along the body before reaching the tail cone.

The final zero-lift coefficient for the fuselage ($C_{D_{0_f}}$) is calculated as 0.0041. This value includes the form drag resulting from the body's profile and a 2.00% installation factor ($K_{install}$) to account manufacturing tolerances and surface discontinuities. Furthermore, the lift-dependent drag coefficient for the fuselage ($C_{D_{L_f}}$) is minimal, calculated at 0.0006 at angle of attack (α) of 6 degrees. The complete set of corresponding parameters and results is shown in Figure 28.

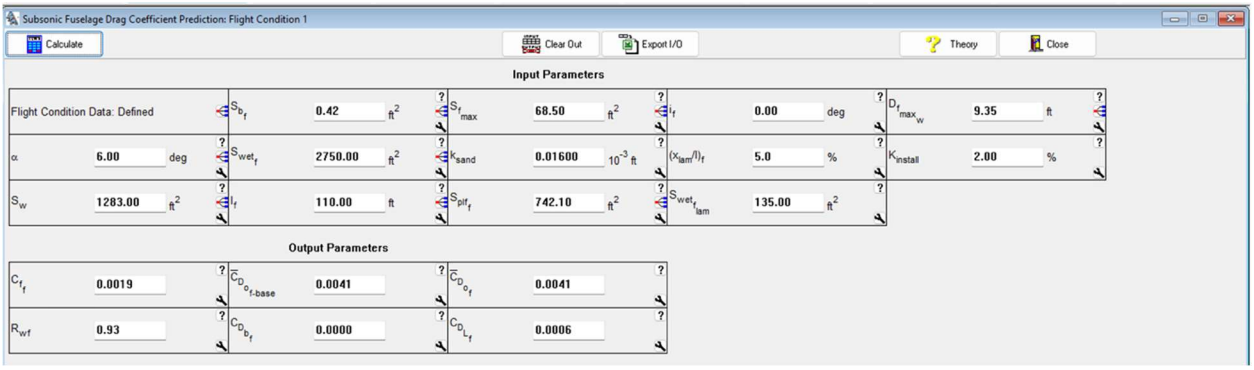

Figure 28: Subsonic Fuselage Drag Coefficient Prediction

4.3. Horizontal Tail

The horizontal tail (HT) is sized and swept to provide the necessary longitudinal stability and control for the aircraft while keeping its drag contribution as low as possible [11]. The HT features an Aspect Ratio (AR_h) of 4.16 and a quarter-chord sweep angle ($\Lambda_{c/4_h}$) of 23.2 degrees. Its total planform area (S_h) is 279.61 ft^2, which is significantly smaller than the main wing, leading to a much lower Reynolds number ($Re_{h_{tur}}$) of 234600.

Despite the small scale, we still assume a fully turbulent boundary layer for the drag estimate. The skin friction coefficient for the tail (C_{f_h}) is calculated at 0.0012. Combining this with the form drag, which is influenced by the 9.00% thickness-to-chord ratio ($(t/c)_h$), the component's zero-lift drag coefficient is a very lean 0.0007.

At the specific flight condition analyzed, where the tail's local lift coefficient (C_{L_h}) is 0.8650, it generates a lift-dependent drag coefficient ($C_{D_{L_h}}$) of 0.1203. While this value appears high relative to its zero-lift drag, it reflects the aerodynamic load required to maintain trim [6]. The Oswald efficiency factor (e_h) of 0.1037 further characterizes the induced drag behavior for this specific tail geometry. The corresponding parameters and results are shown in Figure 29.

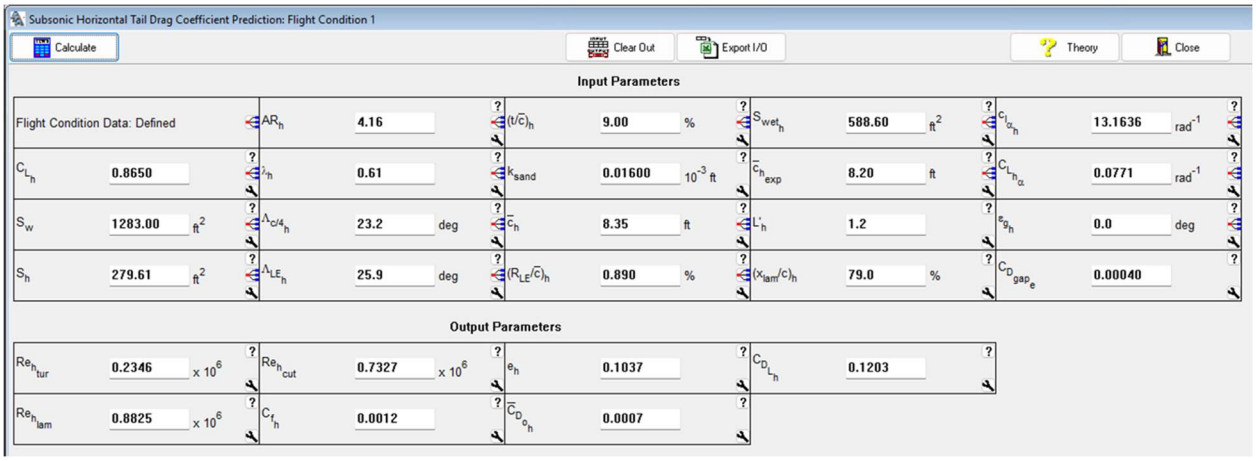

Figure 29: Subsonic Horizontal Tail Drag Coefficient Prediction

4.4. Vertical Tail

The vertical tail is designed primarily to ensure directional stability and yaw control while keeping its drag contribution as low as possible. The geometry reflects a compromise between stability requirements and aerodynamic efficiency. The surface has a relatively low aspect ratio (AR_v = 1.08) and a quarter-chord sweep ($\Lambda_{c/4_v}$) of 37.8°, with a leading-edge sweep (Λ_{LE_v}) of 41.6°. The 9% thickness-to-chord ratio ($(t/c)_v$), provides adequate structural rigidity without significantly increasing form drag, while the high sweep helps delay compressibility effects in cruise [6].

The vertical tail has a planform area (S_v) of 158.88 ft² and a wetted area (S_{wet_v}) of 319.50 ft². At the analyzed flight condition, the turbulent Reynolds number ($Re_{v_{tur}}$) is 1.3985 × 10⁶. Assuming a fully turbulent boundary layer for a conservative estimate, the resulting skin friction coefficient (C_{f_v}) is 0.0027. When viscous and form effects are combined, the zero-lift drag coefficient ($C_{D_{0_v}}$) is calculated to be 0.0008, indicating that the vertical tail contributes only a small portion to the aircraft's overall parasite drag.

For the evaluated condition, the vertical tail operates at a side-force coefficient of 0.8000, producing a lift-dependent drag coefficient ($C_{D_{L_v}}$) of 0.0180. The Oswald efficiency factor (e_v) of 1.2946 reflects the modeling approach and the influence of sweep on the effective span

efficiency. Overall, the vertical tail meets directional stability requirements while maintaining a controlled drag contribution within the total aircraft drag buildup. Figure 30 summarizes the corresponding inputs and results.

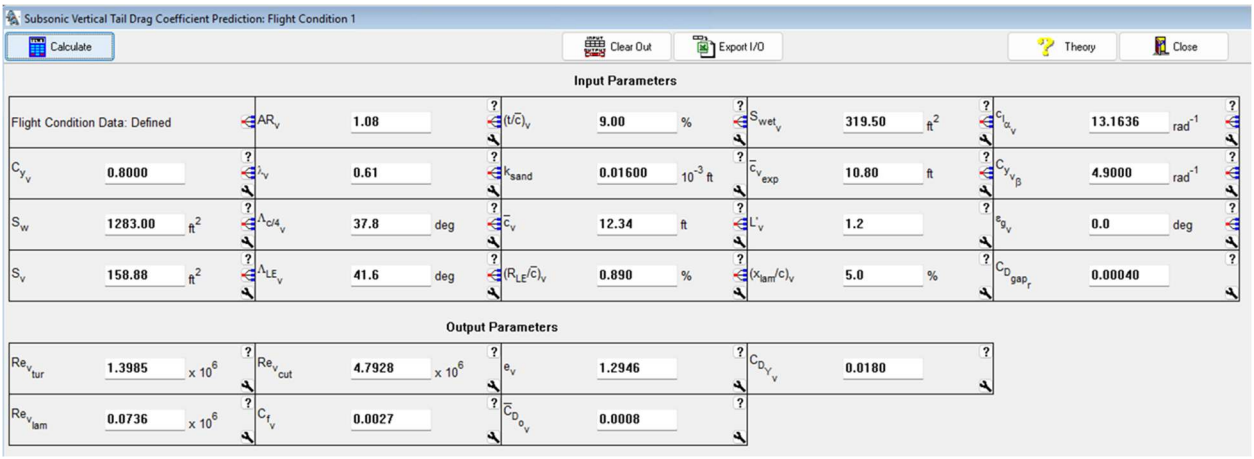

Figure 30: Subsonic Vertical Tail Drag Coefficient Prediction

4.5. Landing Gear

The landing gear drag is analyzed for two primary flight configurations: the cruise phase and the landing phase. For the G700-inspired design, the gear is fully retractable into the fuselage and wing root bays to eliminate parasite drag during high-speed flight. The analysis is based on the specific geometry of a tricycle gear arrangement, including a single nose gear and two main gear assemblies. The physical dimensions for the tires were estimated based on the Goodyear Aircraft Tire Application Guide [12].

The drag breakdown for the gear is as follows and can be found in Figure 31 and 32:

- The main landing gear assembly features dual tires with both front and rear tires areas ($S_{FrontTire}$ and $S_{RearTire}$)of 3.1 ft^2 and a strut length (L_{strut}) of 4.5 ft. This results in a drag coefficient ($C_{D_{gear}}$) of 0.0037 per side.
- The nose landing gear has smaller front and rear tires areas ($S_{FrontTire}$ and $S_{RearTire}$) of 1.1 ft^2 and a strut length (L_{strut}) of 3.5 ft, contributing a drag coefficient ($C_{D_{gear}}$) of 0.0018.

As shown in Figure 31, when the landing gear is retracted, the incremental drag coefficient is 0.0. This reflects a perfectly faired seal where the gear doors are flush with the airframe, ensuring that the total aircraft zero-lift drag is not penalized during the cruise phase.

The landing gear drag is calculated for the extended configuration, representing the significant aerodynamic penalty during the landing phase and takeoff phase. This results in a drag coefficient ($C_{D_{gear}}$) of 0.0037 per side and a nose drag coefficient ($C_{D_{gear}}$) of 0.0018. The total drag coefficient with the gear fully extended is 0.0092, as shown in Figure 32. This reflects the high pressure drag caused by the exposed wheels and structural struts interrupting the otherwise streamlined flow under the fuselage and wings.

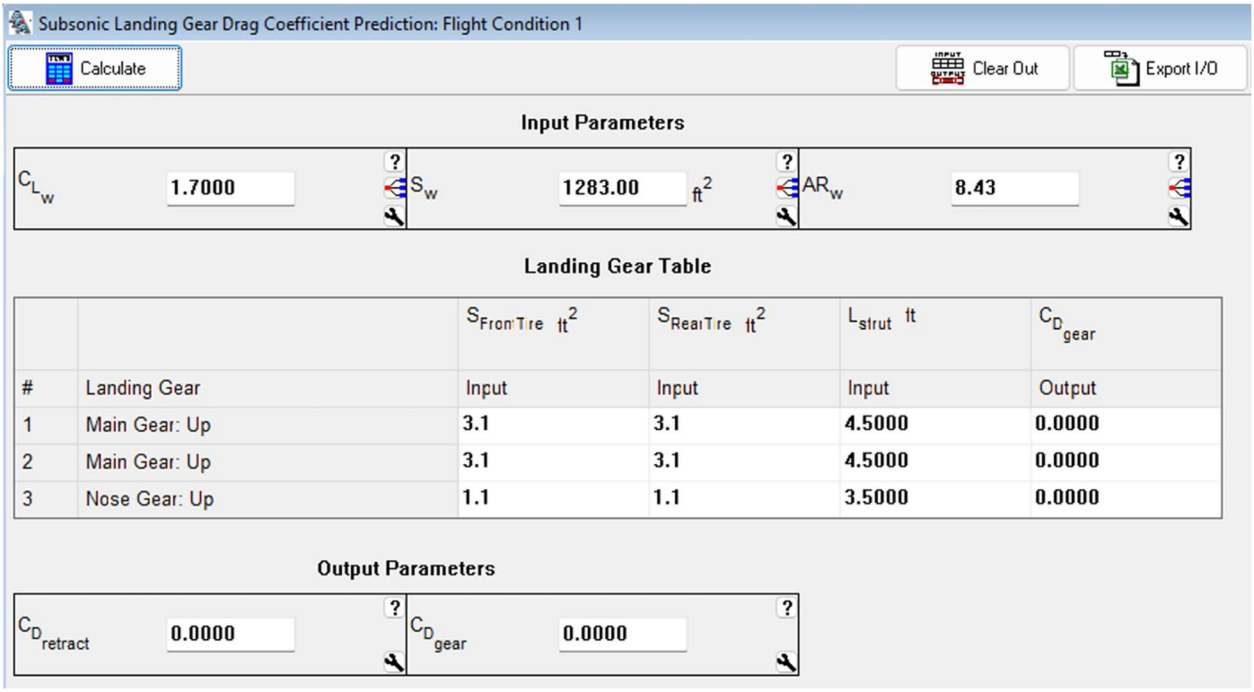

Figure 31: Subsonic Retracted Landing Gear Drag Coefficient Prediction

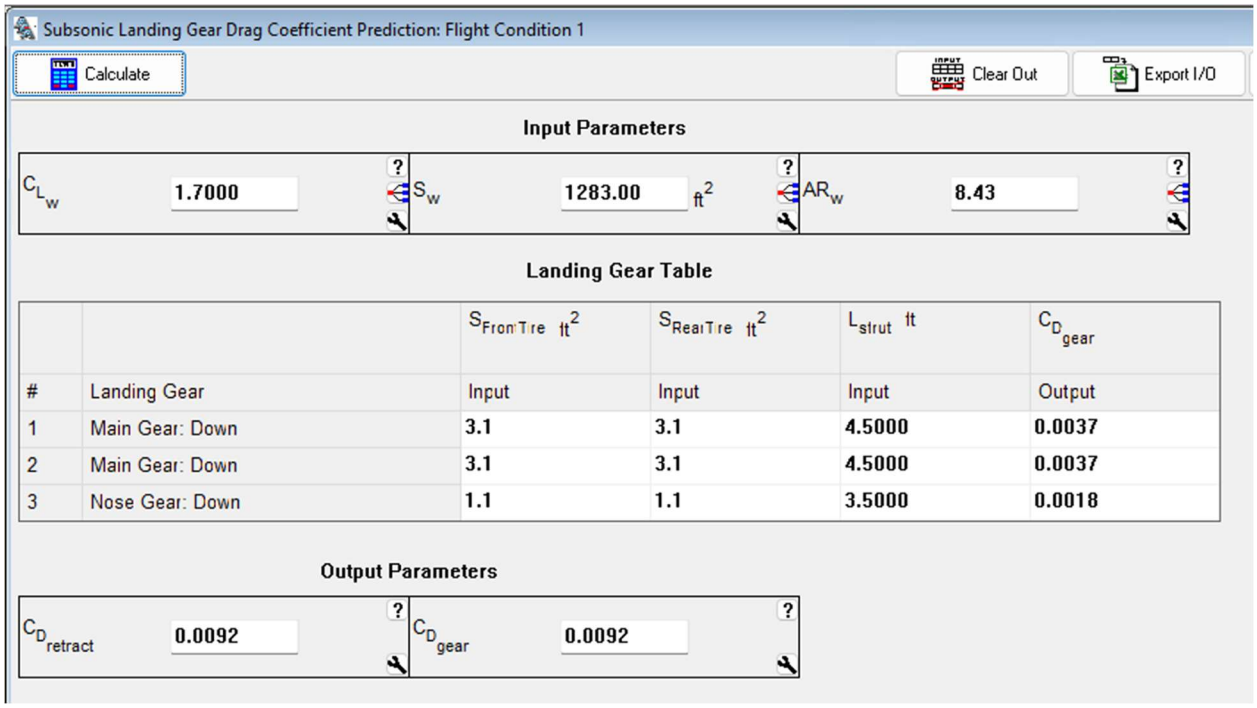

Figure 32: Subsonic Extended Landing Gear Drag Coefficient Prediction

4.6. Nacelles

The subsonic nacelle drag coefficient prediction reveals a symmetrical twin-engine configuration characterized by a longitudinal nacelle length (l_n) of 17.06 ft and a maximum cross-sectional area (S_n) of 30.50 ft^2 per unit. Positioned at a longitudinal station of 74.50 ft and spaced 7.20 ft from the centerline, these nacelles are integrated into the airframe at a 2.50-degree incidence angle to optimize alignment with the local flow field. Based on a total wetted area ($S_{wet_{\Sigma n}}$) of 566.00 ft^2 and a transition point located at 40% of the nacelle length, the analysis calculates a skin friction coefficient (C_{f_n}) of 0.0019 and a pressure drag coefficient of 0.0049 for each unit. When normalized against the reference wing area (S_w) of 1283.00 ft^2 the cumulative impact results in a total nacelle drag coefficient ($C_{D_{\Sigma n}}$) of 0.0101, providing a precise metric for the aerodynamic efficiency penalty associated with the engine installation under these specific flight parameters. The nacelle input parameters were estimated based on geometric data extracted directly from the Gulfstream G700 Aircraft CAD design [4]. Additionally, they can be found in Figure 33 below.

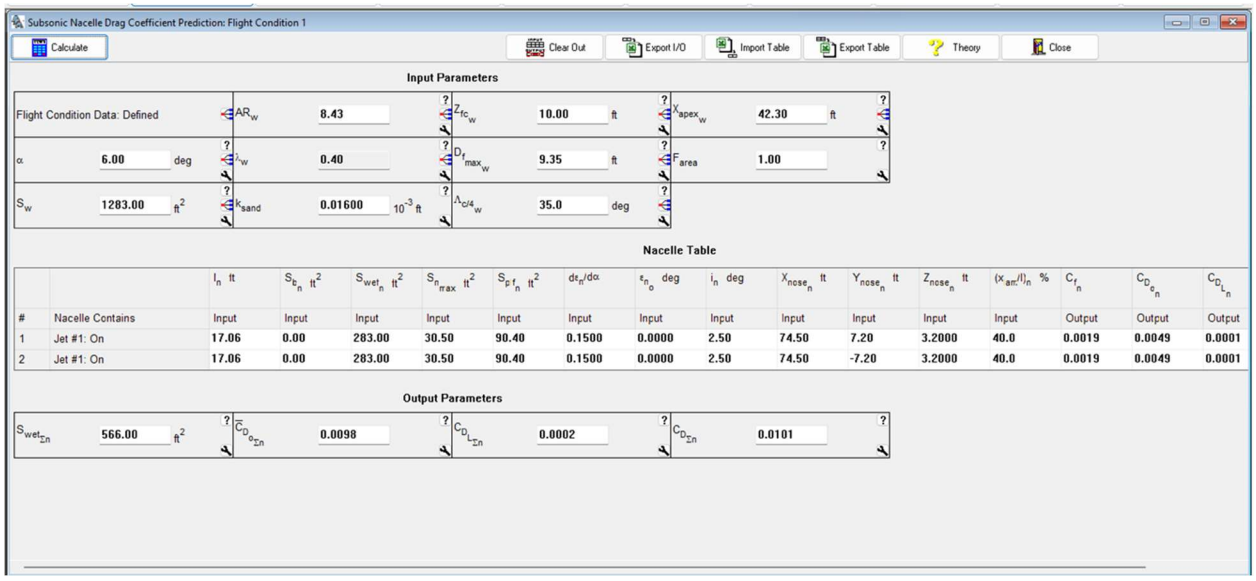

Figure 33: Subsonic Nacelle Drag Coefficient Prediction

4.7. Pylons

The engine pylons are modeled as identical structural units to ensure aerodynamic symmetry and streamlined integration with the rear fuselage. The Each pylon features a quarter-chord sweep angle ($\Lambda_{c/4_{py}}$) of 35.0 degrees and an aspect ratio (AR_{py}) of 0.85. The thickness-to-chord ratio for both units follows a consistent distribution of a mean thickness-to-chord ratio ($(t/c)_{py}$) of 10%. These were calculated using the data extracted from the Gulfstream G700 Aircraft CAD design.[4] Based on this unified geometry, the skin friction coefficient is calculated at 0.0030 for the assembly. The total pylon assembly contributes a zero-lift drag coefficient ($C_{D_{L_{\Sigma py}}}$) of 0.000478. This refined geometry is specifically tailored to mitigate interference drag between the nacelle and the fuselage hull. Furthermore, the identical design ensures a consistent compressibility threshold across both mounts. The input and output parameters of the pylons are displayed in Figure 34 below

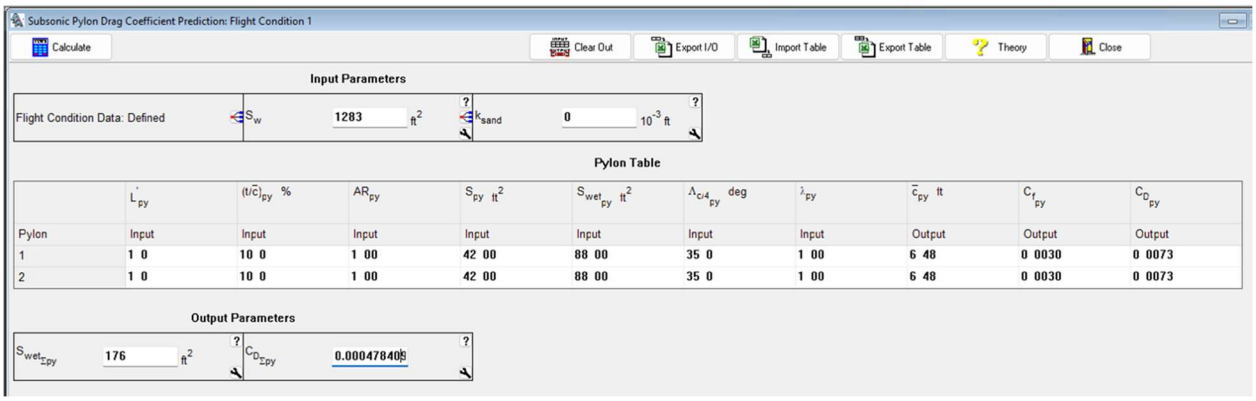

Figure 34: Subsonic Pylon Drag Coefficient

4.8. Windshield

The windshield is a critical area for managing localized pressure gradients and maintaining smooth airflow over the cockpit section [13]. For this design, the windshield is modeled as a double curvature window flush with the surface, a configuration typical of high-end business jets like the Gulfstream G700. This flush-mounted surface is specifically chosen to eliminate the large drag penalties associated with sharp or flat-plate cockpit windows found on older or slower aircraft [c].

The drag increment associated with the windshield is evaluated using a windshield drag increment factor ($\Delta C_{D_{ws}}$) of 0.0020 [14]. When referenced to the wing reference area (S_w = 1283.00 ft²) and accounting for a maximum frontal windshield area ($S_{f_{max}}$ = 68.50 ft²), the resulting drag coefficient contribution is calculated as $C_{D_{ws}}$= 0.0001, as shown in Figure 34.

This very small value confirms that the windshield integration does not significantly penalize the aircraft's zero-lift drag. The smooth geometric blending and absence of sharp frame protrusions effectively limit additional pressure drag [15]. As a result, the windshield contributes only a minor increment to the total aircraft drag buildup while maintaining structural and visibility requirements for the cockpit design [7]. The inputs and outputs parameters of the subsonic windshield drag coefficients are shown in Figure 35 below.

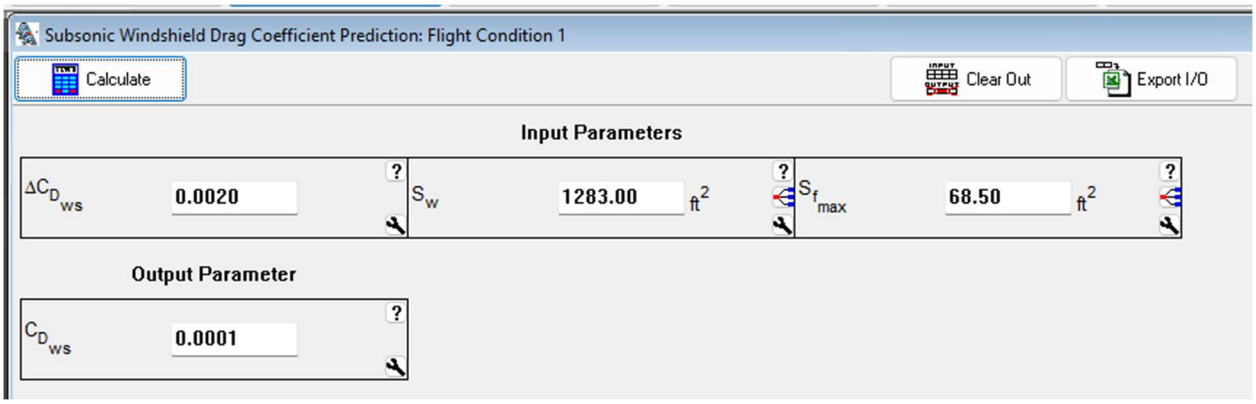

Figure 35:Subsonic Windshield Drag Coefficient Prediction

5. CRITICAL MACH NUMBER FOR WING, HORIZONTAL TAIL & VERTICAL TAIL

Taking the parameters calculated in the geometry and aerodynamic portions of AAA as input, a critical ach number for the horizontal tail, vertical tail, and wing are found. The wing exhibits a critical Mach number (M_{cr_w}) of 0.722. This result is a function of the 35° quarter-chord sweep ($\Lambda_{c/4_w}$), and the 12.00% thickness-to-chord ratio ($(t/c)_w$) justified in the wing section of this report. The horizontal tail demonstrates a higher threshold with a critical Mach number (M_{cr_h}) of 0.803, aided by its thinner 9.00% profile and 23.2-degree sweep ($\Lambda_{c/4_h}$). Similarly, the vertical tail reaches a critical Mach number (M_{cr_v}) of 0.820, benefitting from its aggressive 37.8-degree sweep ($\Lambda_{c/4_v}$) and 9.00% thickness-to-chord ratio ($(t/c)_v$).

The engine pylons show the most significant margins against compressibility. Both pylons have a critical Mach number ($M_{cr_{py}}$) of 0.916. These high limits are achieved using slender profiles, with thickness-to-chord ratios ($(t/c)_{py}$) ranging from 12% at the root to 8% at the tip, alongside sweep angles ($\Lambda_{c/4_{py}}$) of 35.0 degrees. Designing the pylons with these higher thresholds ensures that the complex interference flow between the nacelles and the rear fuselage does not trigger premature wave drag before the rest of the airframe reaches its limits [7].

The engine pylons show the most significant margins against compressibility. Both pylons have a critical Mach number ($M_{cr_{py}}$) of 0.916. These high limits are achieved using slender profiles, with thickness-to-chord ratios ($(t/c)_{py}$) ranging from 12% at the root to 8% at the tip, alongside sweep angles ($\Lambda_{c/4_{py}}$) of 35.0 degrees. Designing the pylons with these higher thresholds ensures that the complex interference flow between the nacelles and the rear fuselage does not trigger premature wave drag before the rest of the airframe reaches its limits [7]

Although the predicted critical Mach numbers are slightly below the target cruise Mach number, this condition is consistent with normal transonic operation, where aircraft routinely cruise above the critical Mach number but below the drag divergence Mach number to balance aerodynamic efficiency and compressibility effects [9]. The AAA values for critical Mach numbers are presented in figure 36 below.

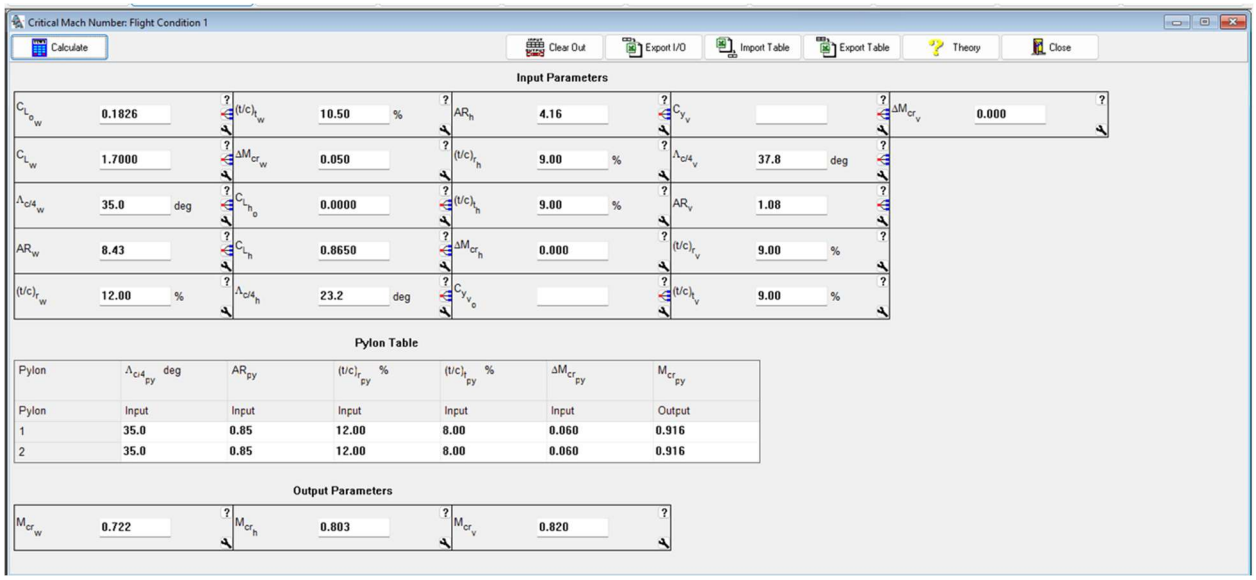

Figure 36:Critical Mach Number for Wing and Empennage

6. CONCLUSION

This report presented the aerodynamic development of a high-speed business jet through analysis of wing geometry, empennage design, lift distribution, drag buildup, and critical Mach number using AAA and supporting tools. The NASA SC(2)-0612 supercritical airfoil was selected to support efficient transonic cruise, while iterative refinement of taper ratio and geometric twist

improved spanwise lift distribution and reduced the risk of tip stall under landing conditions. Symmetrical NACA 0009 airfoils were chosen for the horizontal and vertical tails to ensure stability and control with minimal drag penalties.

The drag buildup demonstrated that the aircraft achieves balanced aerodynamic performance across major components, and the predicted critical Mach numbers confirm suitability for high-subsonic operation within the intended flight regime. Overall, the design process highlights the importance of iterative aerodynamic refinement to balance efficiency, stability, and low-speed handling, providing a solid foundation for further aircraft development.

REFERENCES

[1] C. D. Harris, “NASA supercritical airfoils: A matrix of family-related airfoils,” NASA Technical Publication TP-2969, 1990. [Online]. Available: https://ntrs.nasa.gov/api/citations/19900007394/downloads/19900007394.pdf

[2] Flow5, “Flow5 – Aerodynamic analysis software,” [Online]. Available: https://flow5.tech/flow5.html

[3] B. K. Periyapatna, “Aerodynamics,” course lecture slides, McGill University, Montreal, QC, Canada, Winter 2026.

[4] Autodesk Community Gallery, “Gulfstream G700 Aircraft,” Autodesk, [Online]. Available: Communithttps://www.autodesk.com/community/gallery/project/162351/gulfstream-g700-aircraft?msockid=2ad22e20600f69a725663922615268a3y Gallery

[5] Federal Aviation Administration (FAA), *Airplane Flying Handbook*, FAA-H-8083-3A, U.S. Department of Transportation, 2004. [Online]. Available: https://www.puc.edu/_media/pdf/campus-services/angwin-airport/FAAH80833a-AFH-Ch4-6.pdf

[6] NACA 0009, Airfoiltools.com , http://airfoiltools.com/airfoil/details?airfoil=n0009sm-il

[7] D. P. Raymer, *Aircraft Design: A Conceptual Approach*, 6th ed. Reston, VA, USA: American Institute of Aeronautics and Astronautics (AIAA), 2018

[8] Mohammad H. Sadraey, Aircraft design a systems engineering approach,Wiley,2013

[9] NASA, “Research in Supersonic Flight and the Breaking of the Sound Barrier,” NASA History Office, Washington, DC, USA. [Online]. Available: https://www.nasa.gov/history/SP-4219/Chapter3.html

[10] NASA Glenn Research Center, “Induced Drag,” *NASA Beginner’s Guide to Aeronautics*. [Online]. Available: https://www.grc.nasa.gov/www/k-12/VirtualAero/BottleRocket/airplane/induced.html.

[11] J. G. Leishman, “Aircraft Stability and Control,” *Introduction to Aerospace Flight Vehicles*, Embry-Riddle Aeronautical University. [Online]. Available: https://eaglepubs.erau.edu/introductiontoaerospaceflightvehicles/chapter/aircraft-stability-control/.

[12] Goodyear Aviation, "Aircraft Tire Application Guide," June 2018. [Online]. Available: https://www.goodyearaviation.com/resources/pdf/application-charts-6-2018.pdf.

[13] A. W. Robins, “An investigation of canopy pressures and canopy-fuselage forces,” NASA Langley Research Center, NASA Technical Report. [Online]. Available: https://ntrs.nasa.gov/api/citations/19630002643/downloads/19630002643.pdf

[14] Roskam, D.J.(1997).Airplane Design:Part1 Preliminary Sizing of Airplane, DARcorporation.

[15] J. D. Anderson, *Fundamentals of Aerodynamics*, 6th ed. New York, NY, USA: McGraw-Hill Education, 2017.

CONTRIBUTIONS

- Evelyne Jewitt-Dyck
    - Airfoil selection and schematic, airfoil 2d cl_alpha, wing geometry table and schematic, airfoil selection horizontal tail, horizontal tail planform, horizontal tail aerodynamics, vertical tail airfoil selection and planform, critical mach number for wing horizontal tail and vertical tail, measurements from CAD geometry
- Iris Sam Chacko
    - Airfoil Selection and Xfoil data for wing, Horizontal tail airfoil selection, geometry, aerodynamics and schematics, vertical tail, airfoil selection geometry, aerodynamics and schematics.
- Maverick Hoziel
    - Rationale for wing airfoil, Wing airfoil schematic, wing airfoil cl-alpha, wing geometry table, wing geometry definition schematic, wing twist, wing lift distribution spanwise, Flow5 airfoil analysis
- Milka Ininahazwe
    - Class II Drag calculation (Wing, Fuselage, Horizontal Tail, Vertical Tail, Nacelle, Pylon, Landing gear, Windshield) and Critical Mach number for Wing, Horizontal and Vertical tails